PIV measurements of waves and turbulence in stratified horizontal two-phase pipe flow

M. Birvalski[1], M. Tummers[1], R. Delfos[1] and R.A.W.M. Henkes[1,2]

[1] Laboratory for Aero- & Hydrodynamics, Delft University of Technology, Delft, The Netherlands
m.birvalski@tudelft.nl

[2] Shell Projects & Technology, Amsterdam, The Netherlands

ABSTRACT

The technique for obtaining detailed velocity fields in a wavy liquid layer in stratified air/water pipe flow is described in this paper. By combining Particle Image Velocimetry (PIV) with an interface detection technique, the velocity field is resolved in the whole liquid layer. Furthermore, since the shape of the interface is resolved at each time instance, this information is used to conditionally average the velocity field according to the wave phase, which results in phase-resolved velocity profiles. These velocities are then used to separate the wave-induced motion from the turbulence-induced motion in the liquid layer. In this way, the turbulent wavy regime is analysed. The results of the measurements are compared to the theory of waves and turbulence.

INTRODUCTION

Stratified flow of gas above a liquid layer through closed conduits such as channels or pipes is encountered in many industrial applications. The liquid layer can be either laminar or turbulent, and the interface can be either smooth or wavy. The knowledge of the velocity field of the liquid layer, and the characteristics of the interface, are important both from a scientific as well as from an engineering point of view.

Studies that obtained the velocity profiles in the stratified liquid layer were initially performed in rectangular channels [1-4], and later also in pipes [5-7]. These studies showed that when the interfacial drag is absent, or is very low due to the low air velocity, the liquid velocity profile resembles the profile of a Couette-type flow. The interface in this case acts as a moving wall, dampening the turbulent fluctuations in the surface-normal direction, and slightly enhancing the fluctuations in the surface-parallel direction. When the shear is larger, however, and waves are present on the interface, the velocity profile attains a characteristic S-shape. The turbulent fluctuations show peaks close to the wall due to shear-induced turbulence, but also close to the interface due to fluctuations introduced by the wavy motion.

To distinguish between the velocity fluctuations due to waves from those due to turbulence, the knowledge of the interfacial profile is required. Several studies [8-10] report on techniques that simultaneously acquire the velocity field (by using PIV) and the interfacial profile in flumes or wind-wave tanks. In these studies, two cameras are used: one for capturing PIV images and another that records the interface shape. The PIV camera is positioned below the interface, and angled upwards, while the Profile camera is positioned above the interface, and angled downwards. The interface shape is extracted from the Profile camera images by using an edge detection algorithm, since the illuminated particles in the liquid layer form a sharp edge against the dark background. When both the velocity field and the interfacial profile are known, a phase-averaging procedure can be applied to decompose the velocity field into the time-averaged mean field, the wave-induced motion and the turbulence-induced motion, see e.g. [11, 12].

Thus far, the only study that reports on using PIV in stratified gas/liquid pipe flow is the one by Vestøl and Melaaen [7]. They did not, however, record the interface shape, and therefore the velocity field could not be decomposed. In the present paper, the procedure that combines PIV with interface detection is applied to stratified gas/liquid pipe flow. In this way, the influence of the two main governing phenomena – namely the waves and the turbulence – on the resulting velocity field can be studied separately.

EXPERIMENTAL SETUP

A straight 10.3 m long, 50 mm ID pipe, made of transparent PMMA and high-quality glass (for the PIV test section) was positioned horizontally (see Figure 1, left). The laboratory air was circulated using a fan, and the flowrate was measured with an Instromet turbine flow meter. The water was circulated with a pump, and the flowrate was measured with a Rheonik Coriolis mass flow meter. Both fluids were at atmospheric pressure and temperature. An inlet section was positioned at the entrance which had a Y shape, with water entering horizontally, and air entering at 30 degrees from above. A development length of 150 pipe diameters (7.5 m) was provided before the PIV measurement section. This section, made of Schott Duran glass, included a box-shaped extension (made of regular glass), which corrected for most of the distortions produced by the curved wall of the pipe, and facilitated focusing inside the liquid layer.

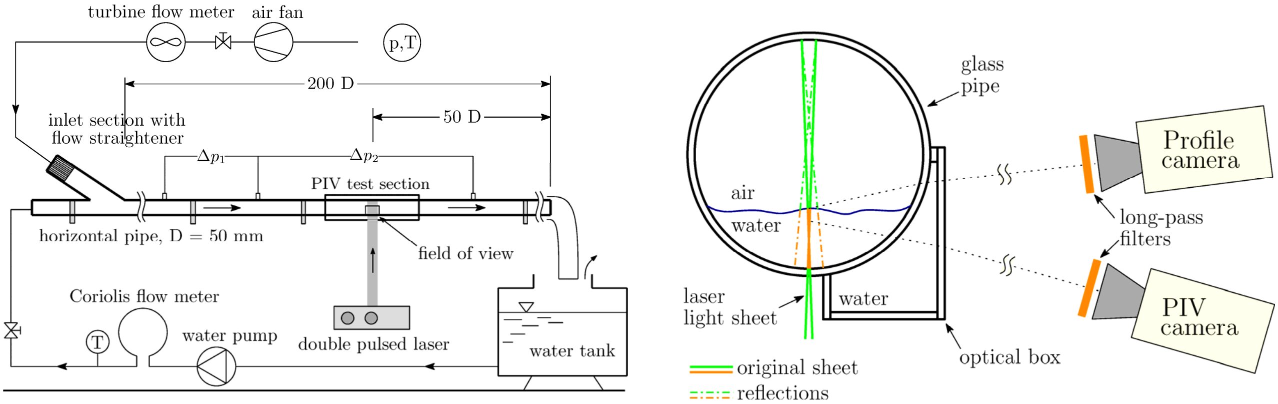

Figure 1 Experimental setup. Schematic view (left) and a cross-section through the PIV test section (right).

The PIV system consisted of a Continuum Minilite Nd:YAG laser (double-shot, 532 nm wavelength, approximately 1.2 mJ/pulse) firing at 2 Hz, a double-frame CCD camera (PCO Sensicam qe, 1376x1040 pixels, 12-bit grayscale) equipped with a 100 mm Tokina lens, and an ILA PIV-Sync synchronizer unit. Like in [8-10], the camera was positioned below the level of the interface and it was set at an angle of approximately 16 degrees, looking upwards underneath the waves (Figure 1, right). This position was necessary to image the whole liquid layer, including the interface, and to avoid any blocking of the view due to waves. The profile capturing was performed with another CCD camera (PCO Sensicam, 1280x1024 pixels, 12-bit grayscale), but positioned above the interface, looking at approximately 7 degrees downwards. The lenses of both cameras were fitted with long-pass optical filters, made from Hoya O56 coloured glass. These filters blocked the green laser light (reflected from the pipe wall and the interface) but transmitted the higher wavelength light emitted by the seeding particles present in the liquid. The material for seeding is a fluorescent pigment from a commercially available acrylic paint, produced by Lefranc & Bourgeois (Flashe Vinyl, fluorescent light orange colour). The pigment particles in this paint have a range of sizes of roughly 1 to 30 µm, with particle agglomerates reaching ~50 µm. Before using them for seeding, the smallest and the largest particles needed to be discarded. This was done by performing two steps of sedimentation. In the first step, the dispersed paint was left to settle over several hours. The sediment, which contained the largest particles, was discarded and the suspension left to settle over a longer period (typically 48 h). After this, the suspension containing the smallest particles was discarded and the sediment was used for seeding.

The light from the laser passed through a set of lenses which shaped it into an approximately 0.5 mm thick and 35 mm wide light sheet in the vertical streamwise plane in the middle of the pipe. The cameras were positioned approximately 40 cm away from the pipe centreline, and their field of view was approximately 25x19 mm^2. A grid of dots (0.5 mm diameter, spaced 1 mm apart), was positioned vertically in the centre plane of the pipe in order to capture the calibration images. An image for the profile camera was taken with the pipe filled with air, and an image for the PIV camera was taken with the pipe filled with water. These images were used to dewarp and scale the captured images, which resulted in corrected images from both cameras that have a common coordinate system.

The PIV images were processed using LaVision's Davis 8 software, by applying a multi-pass, multi-grid, adaptive cross-correlation procedure with the final interrogation area size of 16x16 pixels. The velocities were overlapped by 50%, which resulted in a grid of vectors spaced 0.148 mm apart (the resolution is ~0.0185 mm/pixel). The outliers were detected and eliminated using standard procedures. The final processing step was the application of a mask, generated using the detected interface profile, which sets to zero all the velocity vectors that are outside the liquid layer, i.e. above the air/water interface.

PROFILE DETECTION

A profile detection technique is developed and presented through a series of images shown in Figure 2. Similar algorithms were developed previously by e.g. [8-10] and applied to wave tanks and flumes. We developed the technique further to cope with the small pipe geometry and with the reflections that arise due to the curved walls surrounding the liquid layer.

Figure 2a is a part (700 pixels wide) of an image captured by the Profile camera. The bright area in the lower part consists of images of particles in the light sheet, refracted through the interface. The interface which needs to be detected is seen as a sharp edge in the central part of the image. Besides the interface, two bright spots are seen that lie beyond the edge of the light sheet. These spots are due to light that has been refracted by the interface and then reflected from the top wall of the pipe back onto the liquid layer (see Figure 1, right). This light illuminates the fluid away from the light sheet and, although being much less intense than the original sheet, can create a strong signal if it encounters a large tracer particle on or near the interface. The algorithm, implemented using the Image Processing Toolbox of Matlab (Matlab R2012a, The MathWorks Inc., USA), incorporates steps that correct errors in the detection due to these reflections.

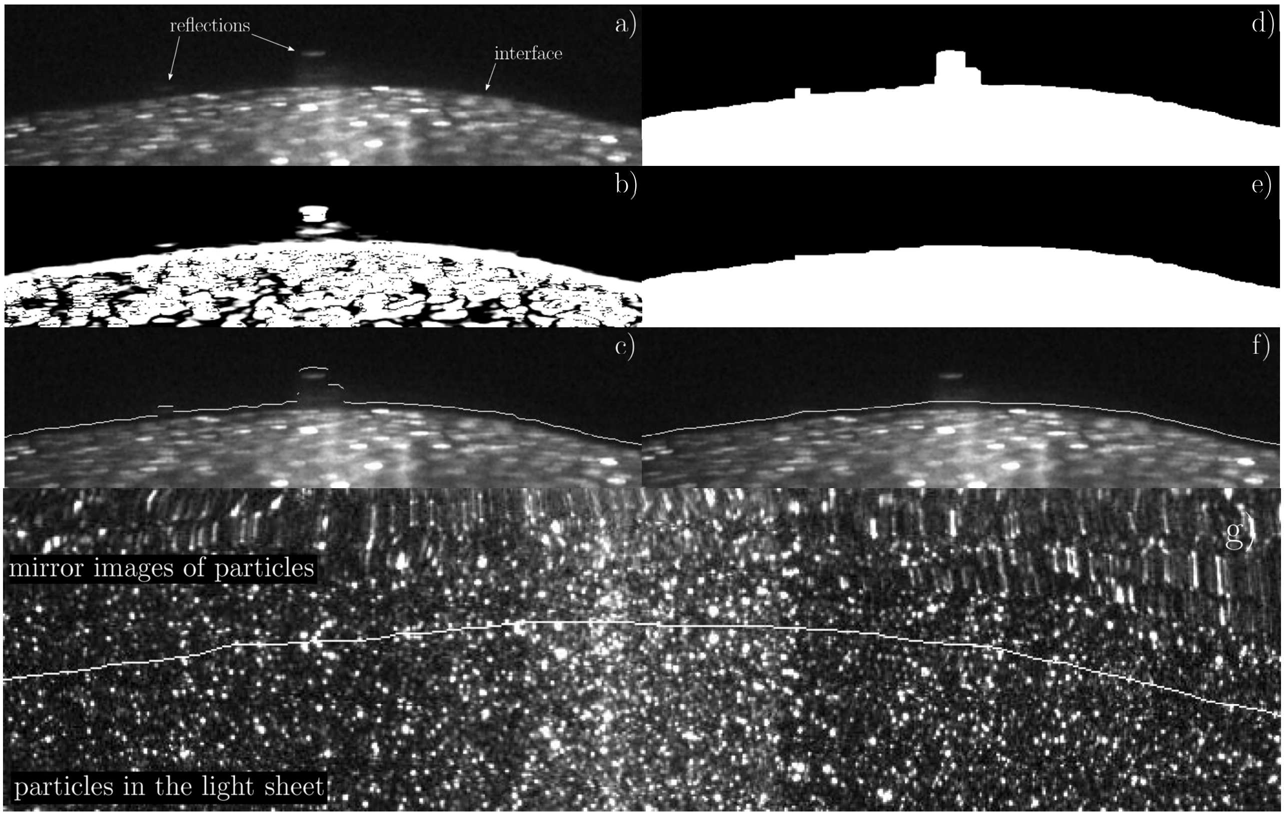

Figure 2 Step-by-step processing of a sample Profile image. a) raw image (detail), b) image after Sobel and Wiener filtering, c) image after thresholding, d) binary representation of the interface, e) interface after opening and closing, f) final profile after smoothing, g) final profile overlaid on the corresponding PIV image (detail).

In the first step, a 3x3 averaging filter is applied to the original image, followed by a vertically oriented Sobel operator, 3x3 pixels in size, which accentuates the edges of the light sheet. Next, a Wiener filter (11x11 pixels) is applied which smoothens the previous result. The absolute value at all pixel positions is calculated and the resulting image is shown in Figure 2b.

Next, a thresholding procedure is applied by scanning the image column by column, starting from the top, and recording the position where a set gradient threshold is exceeded. For this purpose, a variable value threshold is constructed, which has a constant value in the central portion of the image, but linearly changes to a lower value in the first and last (leftmost and rightmost) 300 pixels of the image. This was needed since the light sheet intensity slightly drops towards the edges, and therefore also the gradients calculated by the Sobel operator decrease.

The result of thresholding is seen in Figure 2c. As expected, the off-sheet particles illuminated by the reflections are wrongly marked as the position of the interface. Further steps are needed to correct for this. First, the image is binarised

(Figure 2d) by setting all the pixel values above the interface to zero and those below to one. This produces a shape of the interface with characteristic “notches” which are well suited for correction by applying standard morphological operations such as opening or closing, see e.g. [13].

The opening operation is performed on the binary image using a 60 pixels wide linear horizontal structuring element. The width of the element is chosen to be wider than the “notches” produced by stray light reflecting from the top pipe wall, but narrow enough so that it does not artificially flatten the wave crests. Its effect is seen in Figure 2e.

Occasionally, the algorithm detects the interface below its true position, and therefore produces a “notch” oriented in the other direction. This can occur if the threshold value is too high for the specific column, usually at the edge of the light sheet, where the light intensity is lower. This is corrected by performing a closing operation with a horizontal structuring element, 15 pixels wide.

After the described steps, the profile can contain some discontinuities (i.e. step changes in the interface position), especially in regions where the “notches” were processed by opening or closing. This is finally corrected by applying a moving average, 21 pixels wide, to the detected interface position. The width of this filter (~0.4 mm in physical dimensions), as well as the width of the structuring element used for closing, is kept as low as possible in order to minimise the flattening of the wave troughs, while still achieving the desired effect.

The final detected interface is transformed into real-world coordinates and applied to the corresponding PIV image (Figure 2g). The images of particles in the light sheet and their reflections on the bottom side of the interface are visible and can be used to visually inspect the accuracy of the detected interface profile. It is seen that the detected profile deviates by no more than approximately 3 pixels (~0.06 mm) from the true interface position (assumed to be the locus of the midpoints between particle images and their reflections). In extreme cases, when the spurious reflections are particularly wide, the algorithm may not correct the error fully, and then the deviation from the true interface position can reach up to 10 pixels (~0.185 mm). This is considered satisfactory, since the occurrence of such wide reflections is rare, and therefore does not introduce a significant error in the overall measurement.

PHASE AVERAGING

According to Hussain and Reynolds [11], the velocity beneath the waves can be decomposed into three components: a time-averaged mean velocity, the wave-induced fluctuations, and the turbulence-induced fluctuations:

$$\begin{aligned} &u(x,y,t) = \overline{u}(y) + \tilde{u}(y,\varphi) + u'(x,y,t) \\ &\varphi = f(x,t) \end{aligned} \tag{1}$$

Here, x and y are the horizontal and vertical coordinate in a vertical plane through the pipe centreline. The time-averaged velocity is assumed to depend only on the y coordinate, because the flow in our case changes very little along the axial coordinate x within the field of view (25 mm wide). The wave-induced velocity depends on the y coordinate and on the wave-phase φ.

To determine the wave-phase, a method developed by Siddiqui and Loewen [12] is adapted to the present flow. This method was judged to be suitable for our flow since it can be applied to low-frequency PIV data, like the data collected in our study. The method is based on averaging the velocities on a vertical line beneath a selected phase of the wave.

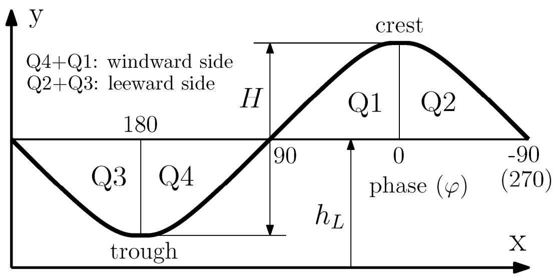

Figure 3 Phase and wave quarter convention. Phase angle in [degrees]. Wave height and mean liquid level are *H* and h_L, respectively. The origin of the coordinate system is fixed to the pipe wall.

After the detection of the interface in all the images, an average value of the liquid height is determined. This average value is applied to each individual profile, resulting in a number of zero-crossings. Waves are composed of a crest region and a trough region, which are located between two zero-crossings each (see Figure 3). A crest and a trough can each be divided into two parts, resulting in wave “quarters”, and their detection is the main goal of this procedure.

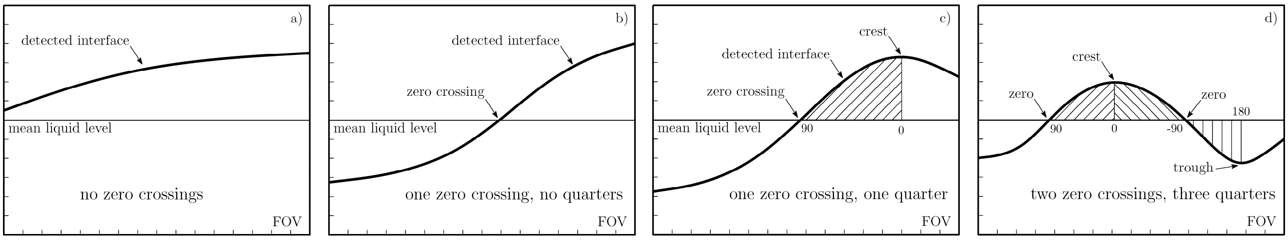

Figure 4 Phase detection technique. The technique, described by Siddiqui and Loewen [12] is based on detecting wave quarters (shaded).

Every detected interfacial profile may contain either no zeros, one zero, or two or more zeros (Figure 4). Profiles without zero crossings cannot be processed (Figure 4a); their number is very small in the current study. Profiles with two or more zeros contain at least one crest or trough i.e. two wave quarters (Figure 4d). The part of the profile between every pair of zeros is scanned for a local maximum (minimum). This point is assigned a phase value (according to the convention shown in Figure 3). Every position in the profile can be assigned a phase by linearly dividing the space between the extreme value (a crest or a trough) and a zero. The profiles with one zero can contain a quarter if a maximum or a minimum is visible as well (Figure 4c). The part of the profile to the left and to the right of a zero is searched for an extreme value, after which it is checked that this value is not on the edge of the image. If the extreme is not on the edge, it is assigned the corresponding phase value. The same procedure is followed when profiles have two or more zeros in the region in front of the first and behind the last zero (Figure 4d). Once the phases of the waves are determined, the velocity profiles at the desired phase can be averaged.

The averaging is done in two coordinate systems. Initially, an Eulerian coordinate system, whose origin is fixed to the pipe wall, is used. When this system is applied to flows with a moving interface, an intermittency factor is included to account for the presence (value 1) or absence (value 0) of e.g. the liquid phase.

The other coordinate system used is suitable for a continuously changing flow structure, like a wavy interface. This system adapts itself to the varying height of the layer by keeping the origin at the pipe wall and the end point at the interface. When averaging the different velocity profiles that belong to the same phase, the height of the profile is divided into an equal number of segments (51 in this study) and the corresponding points are averaged. This ensures that the points on the bottom are averaged with other points on the bottom, and those on the interface with others on the interface. In other words, the points that have the same relative (scaled) height are averaged with each other.

The described method of phase averaging by detecting wave quarters has the following limitations:

$$\begin{array}{ccc} FOV \geq \frac{1}{2}\lambda & \frac{1}{4}\lambda \leq FOV < \frac{1}{2}\lambda & FOV < \frac{1}{4}\lambda \\ \text{fully resolved} & \text{partially resolved} & \text{not resolved} \end{array} \qquad (2)$$

To detect a quarter of a certain wavelength, the quarter needs to be inside the field of view. This means that if the FOV is wider than half of the wavelength (λ), there will always be at least one quarter which can be detected, and therefore that particular wave field can be fully resolved. In our case, waves of 50 mm or less can be fully resolved, since the FOV is 25 mm. As the wavelength becomes longer, however, a smaller and smaller percentage of the profiles will contain detectable quarters, until the wavelength (four times as long as the width of the FOV) for which no quarters can be detected.

Once all the velocity profiles that belong to a certain wave phase are averaged, we have the phase-averaged velocity. It includes a time-averaged component and a wave-induced component:

$$\langle u \rangle (y,\varphi) = \overline{u}(y) + \tilde{u}(y,\varphi) \qquad (3)$$

Now we can use Eq. (1) to calculate the turbulent contribution and Eq. (3) to calculate the wave-induced motion, after we have calculated the time-averaged velocity in the same adaptive coordinate system. In this way, all the components of the velocity field are obtained.

RESULTS

One turbulent wavy case is analysed next, using the described profile detection and velocity decomposition methods. The superficial air and water velocities were set to 5.4 m/s and 0.026 m/s, respectively, and 3000 images were recorded at 2 Hz, ensuring the samples are uncorrelated.

The bulk flow properties and the interface statistics are presented in Table 1. The Reynolds numbers were calculated using the real bulk velocities, and the hydraulic diameter. Their values, and the turbulent structures that are observed in the instantaneous PIV images, suggest that both phases are turbulent.

Table 1 Flow properties and interface statistics.

Air velocity (superficial), u_{SG}	5.4 m/s	Average crest length (Q1+Q2), l_c	12.03 mm
Water velocity (superficial), u_{SL}	0.026 m/s	Average trough length (Q3+Q4), l_t	11.18 mm
Reynolds number, air, Re_G	18557	Av. windward slope length (Q4+Q1), l_w	12.38 mm
Reynolds number, water, Re_L	4069	Av. leeward slope length (Q2+Q3), l_l	10.83 mm
Number of samples, N	3000	Average crest height, H_c	+0.65 mm
Number of crests, n_c	3812	Average trough height, H_t	-0.74 mm
Number of troughs, n_t	3984	Average wave height, H	1.39 mm
Mean liquid level, h_L	8.54 mm	Average crest steepness, s_c	0.054
Average wavelength, λ	23.21 mm	Average trough steepness, s_t	0.066

The measured wavelength of 23.21 mm reported in Table 1 is below the theoretical limit of 50 mm for our configuration, and the waves are thus fully resolved. The wave statistics show that the crests are slightly longer than the troughs, and that the troughs have a larger height than the crest. As a result, the troughs are steeper than the crests. This is indicative of the capillary-gravity wave type, in which the waves attain such a shape due to the strong influence of the capillary forces.

The data presented in Table 1 are derived from the lengths and heights of all the wave quarters detected in the images. These quarters are shown in Figure 5, where their length is plotted against their height (positive if they belong to crests, and negative if they belong to troughs). There is a wide distribution of both lengths and heights, which is expected since the waves arise naturally due to air shear, and since the turbulence in the liquid layer acts to degrade the regularity of any wavy pattern present on the interface.

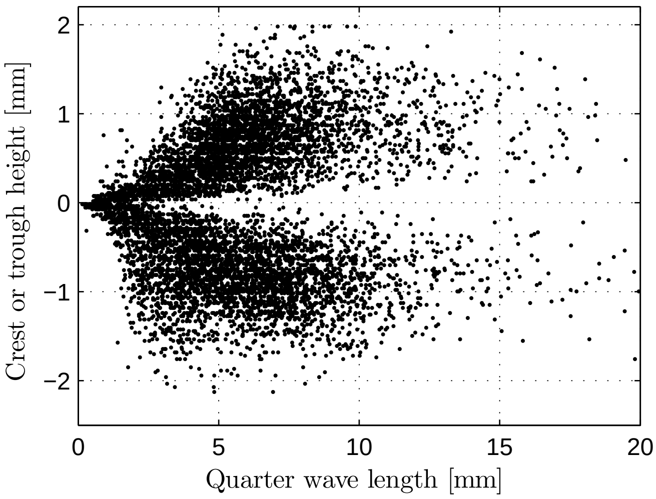

Figure 5 All the wave quarters detected in the Profile images. Crests have a positive height, and troughs have a negative height. In total, 7796 quarters were detected.

To study the velocities inside the liquid layer, the Eulerian coordinate system is employed first. The average axial and radial velocities and the Reynolds stresses are presented in Figure 6. The axial velocity has the characteristic S-shaped profile, which deviates from the logarithmic shape seen in boundary layers due to the influence of waves. The radial velocity (presented in the same plot, but multiplied by 10) shows a slight positive average velocity, indicating the presence of secondary flow directed upwards, towards the interface. The Reynolds stresses (axial, radial and shear, scaled by the friction velocity derived by fitting a line through velocity points in the viscous sublayer) show the same behaviour close to the wall as single-phase boundary layer flows. For example, the value of 2.7 is reached by the scaled axial Reynolds stress, which is a value reached in single-phase flow through pipes as well [14]. However, further away from the wall, the velocity induced by the waves is substantial, and forms the major part of the reported fluctuations. This is confirmed also by the fact that the fluctuations reach a peak just underneath the interface, where the wave-induced velocities are highest.

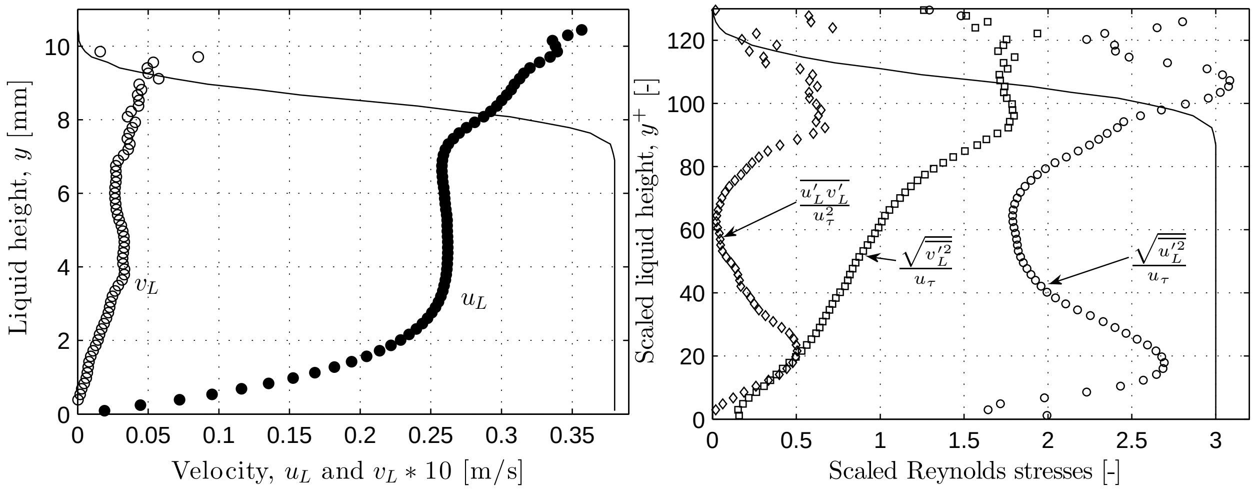

Figure 6 Axial and radial velocity (left), and scaled Reynolds stresses (right) presented using an Eulerian coordinate system with the origin at the pipe wall. The solid line is the intermittency function.

To separate the velocities induced by the waves from those induced by the turbulence, phase averaging followed by velocity decomposition is performed next, using the adaptive coordinate system.

Starting from the crest, the velocity is phase-averaged in 10 phase degree steps, covering the entire wave profile (360 degrees). Also, the average height and axial distance from the crest at a particular phase angle are calculated. This results in phase-averaged velocities underneath a measured average wave profile. The axial and radial phase-averaged and wave-induced velocities are presented in Figure 7. The wave-induced velocity was obtained by subtracting a time-averaged mean velocity (calculated in the adaptive coordinate system) from the phase-averaged velocity.

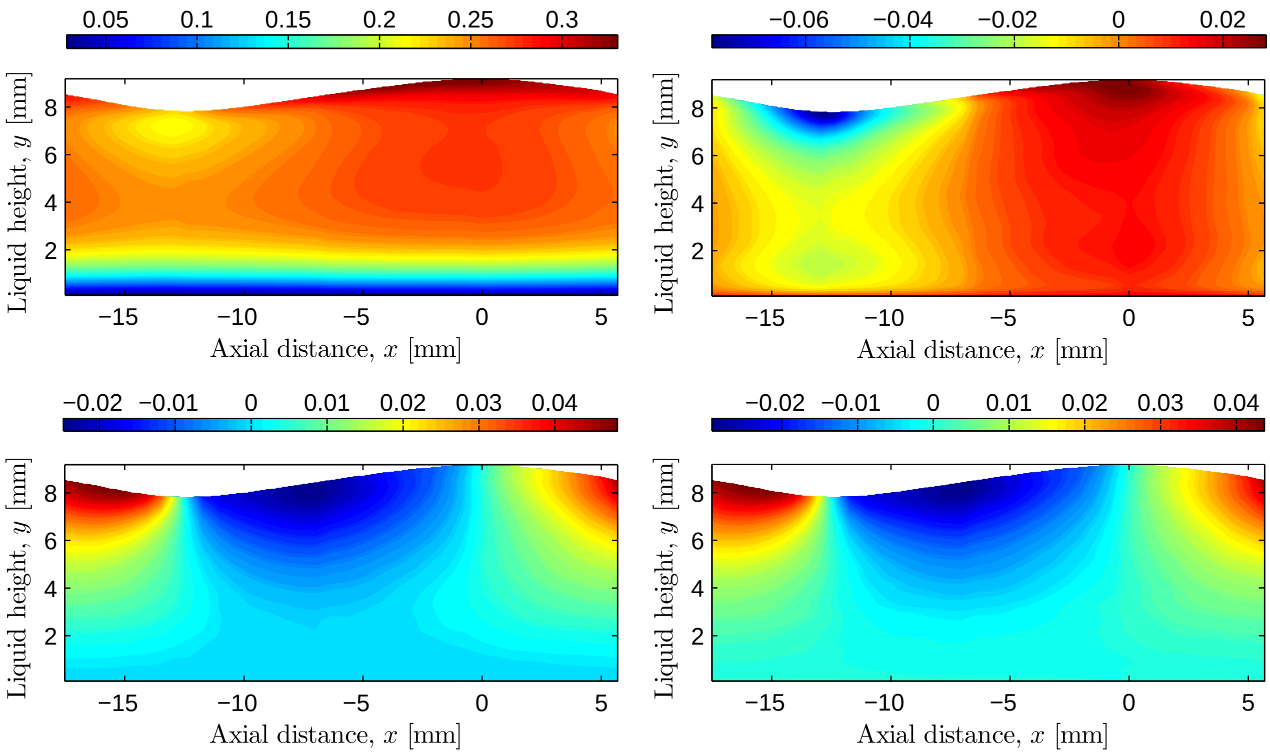

Figure 7 Phase-averaged (left column) and wave-induced (right column) axial (top row) and radial (bottom row) velocities [m/s].

As expected, there is a high axial velocity area below the crest and a low velocity area below the trough. This is especially prominent in the wave-induced velocity plot, where the mean velocity of the flow was subtracted. The wave-induced velocity magnitude is higher below the trough than below the crest and this is attributed to the higher steepness of the trough (Table 1). Radial velocity in the flow is mainly induced by the waves, as little difference can be seen between the phase-averaged and the wave-induced velocity plots. The radial velocity is highest close to the zero-crossings (phase angles 90 and 270), with the velocity on the leeward slope higher than the one on the windward slope. This difference is caused by the leeward slope being steeper than the windward slope (the waves are skewed in the direction of the flow), which is likely caused by the shear, present in the mean flow.

The axial and radial turbulent fluctuations, obtained by decomposing the velocity field, are presented in Figure 8. As can be seen, the separation of turbulent motion from the wavy motion is only partially successful. Namely, the high turbulent fluctuations close to the interface in both the axial and the radial direction cannot entirely be attributed to turbulence, but are likely caused by wave motion. As shown in Figure 5, the waves have a range of lengths and heights, and therefore induce different velocities in the liquid layer. The difference between these velocities and the phase-averaged velocity would not be detected as wave motion, but as turbulence.

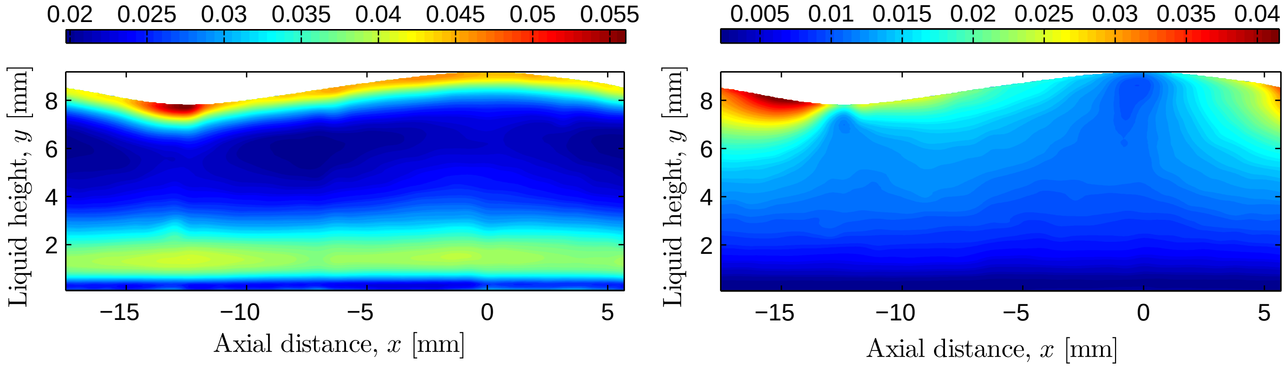

Figure 8 Root-mean-square value of axial (left) and radial (right) turbulent fluctuations [m/s].

To clarify this further, we divide the detected waves into 3 categories according to their steepness (H/λ, presented in Figure 9, left). Group 1 is the steepest, containing waves steeper than 1.5 times the average of all the quarters detected for a particular phase. Group 2 contains waves of steepness between 0.5 and 1.5 times the average, and group 3 consists of waves with steepness less than 0.5 times the average. The phase-averaging is performed for phase angles 0 (crest) and 180 (trough), and axial velocity shown in Figure 9 (middle and right). As can be seen, the different groups have different phase-averaged and wave-induced velocities. As expected, the steepest group has the highest increase (decrease) of velocity below the crest (trough) compared to other groups. This means that waves induce velocities in a systematic manner, which is governed largely by the wave steepness (as also predicted by e.g. linear wave theory [15]). If we consider that each group consists of waves that are different from each other and therefore induce different velocities, it is clear that this causes error by appearing as turbulence, and not as wave-induced motion. This effect is strongest where the wave-induced velocity is highest, i.e. at the trough in case of axial velocity, and at the zero-crossings in case of radial velocity (see Figure 8). The rest of the turbulent fluctuation profile contains erroneous wave-induced velocity contributions as well, but to a lesser degree.

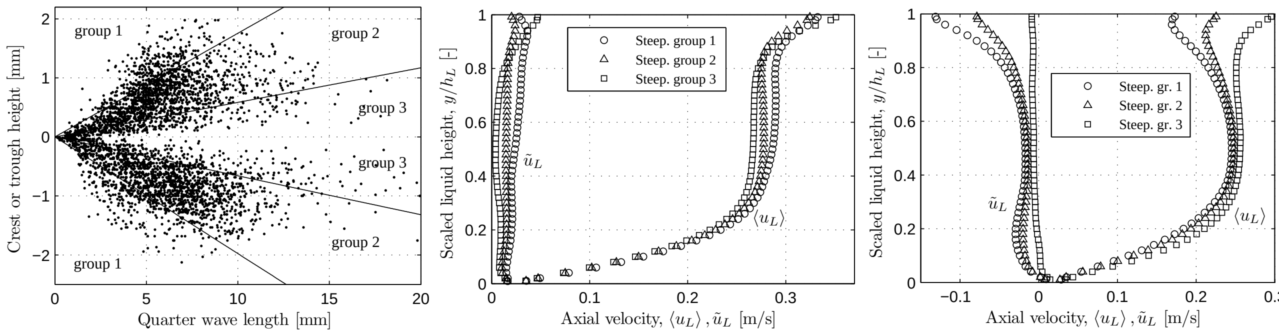

Figure 9 Left: Detected quarters divided into groups according to steepness from steepest (group 1) to least steep (group 3). Middle: Phase-averaged and wave-induced axial velocity profiles of the three steepness groups, at phase angle 0 (crest). Right: Phase-averaged and wave-induced axial velocity profiles of the three steepness groups, at phase angle 180 (trough).

Since the present velocity decomposition method determines the wave-induced velocity by averaging the experimental profiles at a specified wave phase, it is also susceptible to another kind of error. Namely, if the turbulent events (bursting, in-sweep) occurring at the wall correlate with the waves at the interface, the velocity resulting from these events will be included into the wave-induced motion. Consequently, the turbulent fluctuations at positions where the wave-turbulence interaction occurs will be reduced.

A way to solve this problem would be to obtain the wave-induced velocities from a nonlinear stream function, like in e.g. [16]. However, this would only be a partial solution, since the flow is neither two-dimensional nor irrotational, as assumed in this method. Furthermore, additional error would be introduced into the decomposed velocity field if there is also wave-turbulence interaction in the other direction, i.e. if the turbulence influences the shapes of the waves.

In our flow, in which the scales of waves and turbulence are comparable to each other, wave-turbulence interaction in both directions is expected. Because of this, only partial velocity decomposition can be achieved.

CONCLUSIONS

A method for studying waves in stratified air/water pipe flow was developed and data for one turbulent wavy case were presented. The method combines PIV with a Profile detection technique to simultaneously obtain the velocity field in the vertical plane through the pipe centreline, along with the interfacial profile. The velocity is decomposed into three components, using a phase-averaging method that averages velocities that lie on a vertical line beneath a selected wave phase. The waves are found to be irregular (belonging to the capillary-gravity type) and to possess a range of wave lengths and heights. Due to this, and due to the likely presence of wave-turbulence interaction, the separation of different velocity components is possible only to a certain degree.

REFERENCES

[1] Akai, M., Inoue, A., Aoki, S., Endo, K., 1980. A co-current stratified air-mercury flow with a wavy interface. Int. J. Multiphase Flow, 6, 173-190.

[2] Fabre, J., Masbernat, L., Suzanne, C., 1987. Stratified flow, Part I: local structure. Multiphase Sc. and Technol., 3, 285-301.

[3] Lorencez, C., Nasr-Esfahany, M., Kawaji, M., Ojha, M., 1997. Liquid turbulence structure at a sheared and wavy gas-liquid interface. Int. J. Multiphase Flow, 23(2), 205-226.

[4] Fernandino, M., Ytrehus, T., 2008. Effect of interfacial waves on turbulence structure in stratified duct flows. J. Fluid Eng.-T. ASME, 130, 061201(1-8).

[5] Paras, S.V., Karabelas, A.J., 1992. Measurements of local velocities inside thin liquid films in horizontal two-phase flow. Exp. Fluids, 13, 190-198.

[6] Strand, Ø. 1993. An experimental investigation of stratified two-phase flow in horizontal pipes. PhD Thesis, University of Oslo, Norway.

[7] Vestøl, S., Melaaen, M., 2007. PIV and gamma measurements of stratified unprocessed gas flow in a horizontal and near horizontal test pipe. Proc. 13th Int. Conf. on Multiphase Prod. Technol., 237-250.

[8] Peirson, W.L., 1997. Measurement of surface velocities and shears at a wavy air-water interface using particle image velocimetry. Exp. Fluids, 23, 427-437.

[9] Mukto, M.A., Atmane, M.A., Loewen, M.R., 2007. A particle-image based wave profile measurement technique. Exp. Fluids, 42, 131-142.

[10] Siddiqui, M.H.K., Loewen, M.R., 2007. Characteristics of the wind drift layer and microscale breaking waves. J. Fluid Mech., 573, 417-456.

[11] Hussain, A.K.M.F., Reynolds, W.C., 1970. The mechanics of an organized wave in turbulent shear flow. J. Fluid Mech., 41(2), 241-258.

[12] Siddiqui, K., Loewen, M.R., 2010. Phase-averaged flow properties beneath microscale breaking waves. Boundary-Layer Meteorol., 134, 499-523.

[13] Gonzales, R.C., Woods, R.E., Eddins, S.L., 2009. Digital image processing using MATLAB. Second Edition, Gatesmark Publishing, USA. ISBN: 978-0-9820854-0-0.

[14] Eggels, J.G.M., Unger, F., Weiss, M.H., Westerweel, J., Adrian, R.J., Friedrich, R., Nieuwstadt, F.T.M., 1994. Fully developed turbulent pipe flow: a comparison between direct numerical simulation and experiment. J. Fluid Mech., 268, 175-209.

[15] Dean, R.G., Dalrymple, R.A., 1998. Water wave mechanics for engineers and scientists. World Scientific Publishing Co. Pte. Ltd. ISBN 9810204205.

[16] Jiang, J.-Y., Street, R.L., Klotz, S.P., 1990. A study of wave-turbulence interaction by use of a nonlinear water wave decomposition technique. J. Geophys. Res., 95, 16037-16054.